

ORIGINAL ARTICLE

Open Access



# Achieving High Strength-plasticity of Nanoscale Lamellar Grain Extracted from Gradient Lamellar Nickel

Zimeng Wang, Yunfei Jia<sup>\*</sup> , Yong Zhang, Pei Tang, Xiancheng Zhang<sup>\*</sup> and Shantung Tu

## Abstract

Traditional metallic materials usually face a dilemma between high strength and poor strain hardening capacity. However, heterogeneous structured metallic materials have been found to obviously overcome the trade-off. Herein, gradient lamellar structure was fabricated through ultrasound-aided deep rolling technique in pure Ni with high stacking fault energy after heat treatment. The gradient lamellar Ni was successively divided into the four regions. In-situ micropillar compression tests were conducted in different regions to reveal the corresponding microscopic mechanical properties. Microscopic characterization techniques were performed to explore underlying deformation mechanisms and the effects of microstructural parameters on deformation behaviors. This work demonstrates that the micropillar with near nanoscale lamellar thickness possesses excellent strength and plasticity. On one hand, the reason for high strength of near nanoscale micropillar is that the strength of micropillar increases with the decrease of lamellar thickness according to the Hall-Petch effect. On the other hand, numerous lamellar grain boundaries perpendicular to the loading direction is found to hinder the motion of slip bands, resulting in great strain hardening capacity in the near nanoscale lamellar micropillar.

**Keywords:** Nanoscale lamellar structure, Compression test, Slip, Dislocation

## 1 Introduction

Nowadays, metallic materials with high strength or even the theoretical strength is fabricated extensively via refining grains into ultrafine-scale or nano-scale. However, ultrafine grain (UFG) and nanograin (NG) metallic materials are often accompanied by limited plasticity resulting from the lack of strain hardening capability [1–4]. The strain hardening is caused by the continuous multiplication and accumulation of dislocations during deformation, which are mostly annihilated in UFG and NG metallic materials due to the dislocation absorption by abundant grain boundaries (GBs) or free surface. To resolve the trade-off between strength and plasticity

of the UFG and NG metallic materials, a great number of studies [5–10] have been devoted to heterogeneous nanostructured metals (HNMs) possessing a superior combination between high strength and good plasticity.

HNMs refer to metallic materials with dramatic distinction in strength between different domain areas [11]. Special attention has been paid on the representative HNMs [10], such as gradient microstructure, gradient lamellar structure, bimodal structure, harmonic structure, dispersed nanodomains, etc. These HNMs have been widely fabricated by severe plastic deformation (SPD) techniques. For instance, Wu et al. [8] reported the gradient sample produced by surface mechanical attrition treatment (SMAT) in interstitial free steel, which presents a unique extra strain hardening when yield stress is much higher than that of homogeneous coarse grain (CG) sample. Another representative HNM work studied by Wu et al. [12] is

\*Correspondence: yfjia@ecust.edu.cn; xc Zhang@ecust.edu.cn

Key Laboratory of Pressure Systems and Safety, Ministry of Education, School of Mechanical and Power Engineering, East China University of Science and Technology, Shanghai 200237, China

heterogeneous lamellar structure fabricated by asymmetric rolling (ASR) and partial recrystallization in Ti, with an excellent property combination of near-NG strength, near-CG ductility and relatively high strain hardening. Moreover, a NG Cu–10Zn layer sandwiched between two CG Cu layers produced by Ma et al. [9] was processed by high-pressure torsion (HPT) technique, and exhibits high strain hardening due to mechanical incompatibility between different layers. Song et al. [13] pointed out that after treated by equal channel angular extrusion (ECAE/ECAP), a 12Cr steel with bimodal structure was hardened up to ~ 35%. In addition, Liu et al. [14] proposed that nano-lamellar microstructure processed by surface mechanical milling (SMGT) obviously enhanced the strength and maintained good thermal stability.

In spite of the abundant successes in producing HNMs through the SPD techniques mentioned above, only few researches have been reported about ultrasound-aided deep rolling (UADR) technique fabricating HNMs. UADR is a SPD technique adopted to strengthen metal surface by grain refinement through introducing remarkable strain gradient along the surface [15–17]. In addition, there are lots of publications investigating macroscale mechanical properties of HNMs [18–24]. However, the microscale deformation behaviors of different regions in HNMs are less well explored, which are worth studying respectively and independently. This contributes to understanding the effects of microstructural parameters in each region on microscale deformation behaviors of microscopic samples, which helps the design of microstructure for metallic materials achieving the synergy of strength and plasticity. The reason for the lack of respective research in different regions may be that conventional experimental methods are unavailable to perform microscale mechanical characterization and tests on microscale samples.

In the present paper, pure nickel (Ni) with high stacking fault energy has been subjected to UADR technique to fabricate gradient lamellar microstructure after heat treatment. In-situ micro-compression tests were conducted to thoroughly investigate the microscale deformation behavior of different regions of gradient lamellar Ni. The corresponding stress-strain curves show that micropillars with smaller lamellar thickness grains exhibit higher yield stress and greater strain hardening capacity than with larger lamellar thickness grains or single grain. Transmission electron microscopy (TEM) characterization technique was used to compare the differences in dislocation and slip evolution between each micropillar in different regions after in-situ compression tests, which attempted to clarify the underlying deformation mechanisms of different regions and the effects of

microstructural parameters on mechanical properties of gradient lamellar Ni.

## 2 Experimental Methods

### 2.1 Overview

The main procedure of this work is clearly illustrated as the schematic image in Figure 1. First, the raw material was processed by UADR technique after heat treatment. Then, the UADRed macroscopic sample was characterized through some microstructural characterization techniques such as electron back scatter diffraction (EBSD), scanning electron microscope (SEM) and so on. Thus, the location of regions with different microstructure could be acquired, which provided the base of micropillar sample preparation in different regions. After different micropillars were fabricated by Focus ion beam (FIB) technique, in-situ compression tests would be performed to obtain mechanical behaviors of these micropillars. Finally, the TEM samples were processed from compressed micropillars through FIB technique, and then transferred to copper stage by using Pt deposition technique for further TEM characterization. More details and parameters are described in the following chapters.

### 2.2 Materials and Fabrication Method

The material used in this work is Ni with a purity of 99.9 wt.%, and its chemical composition (Table 1) is measured using energy dispersive spectrometer (EDS) analysis. A polycrystalline Ni rod with a diameter of 10 mm and a length of 100 mm was annealed at 1000 °C for 10 h in vacuum to encourage grain growth and homogenization, which was then subjected to UADR at ambient temperature.

The working principle of UADR is that working head exerts a certain amplitude of ultrasonic vibration on metallic material surface along normal direction and simultaneously feeds along the uniaxial direction, which induces normal stress to refine grains and shear stress to elongate grains on the metallic material surface [25–27]. During the UADR processing, which is shown in Figure 2, the annealed rod sample rotates at a velocity of 250 r/min, while a steel ball penetrates into sample surface and rolls along axial direction at a velocity of 10 mm/min. The amplitude of ultrasonic vibration of steel ball ranges from 12 μm to 14 μm with vibration frequency of 17.5–18.8 kHz. The sample is considered as being treated by one pass as the tool tip rolls from one end of the rod surface to the other end. To increase the plastic strain, the sample was treated by five passes with loads of 80 N, 100 N, 120 N, 140 N and 160 N, respectively. Cooling oil was used for temperature control during processing.

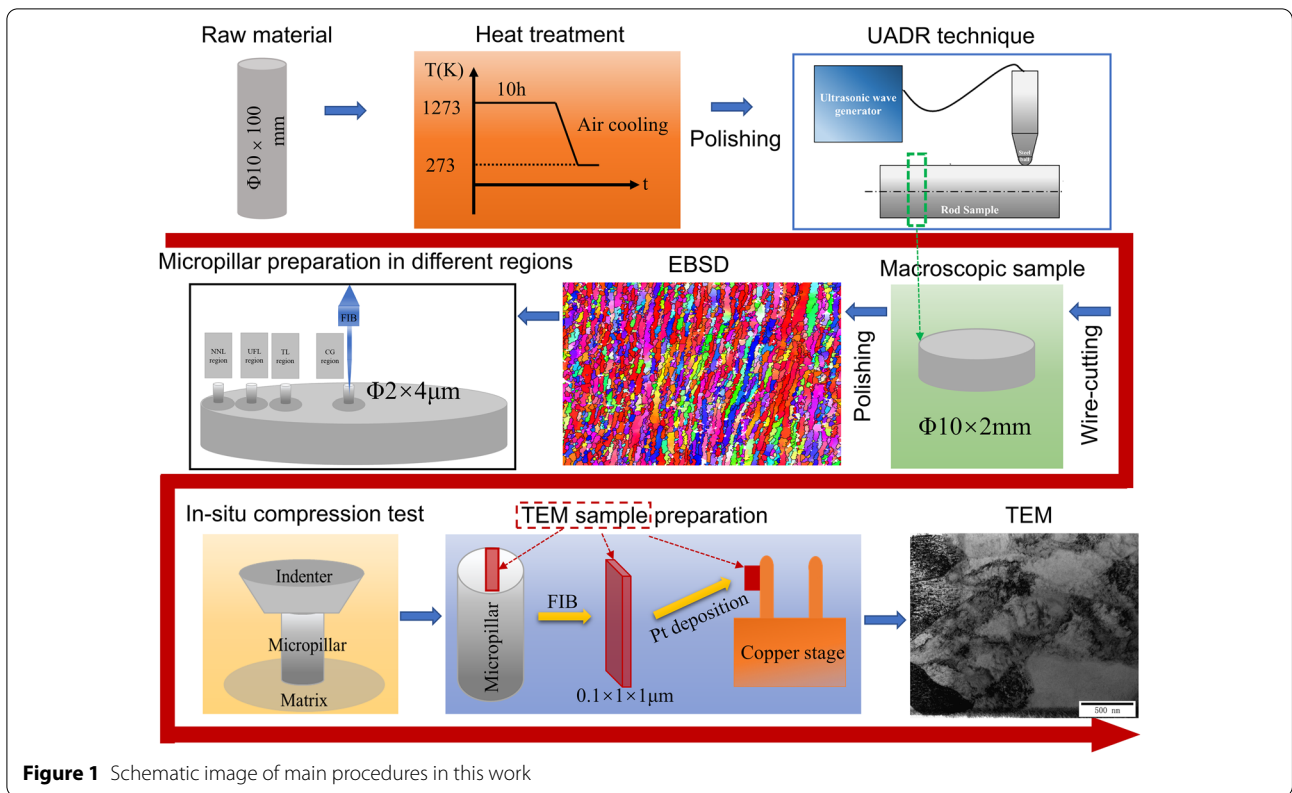
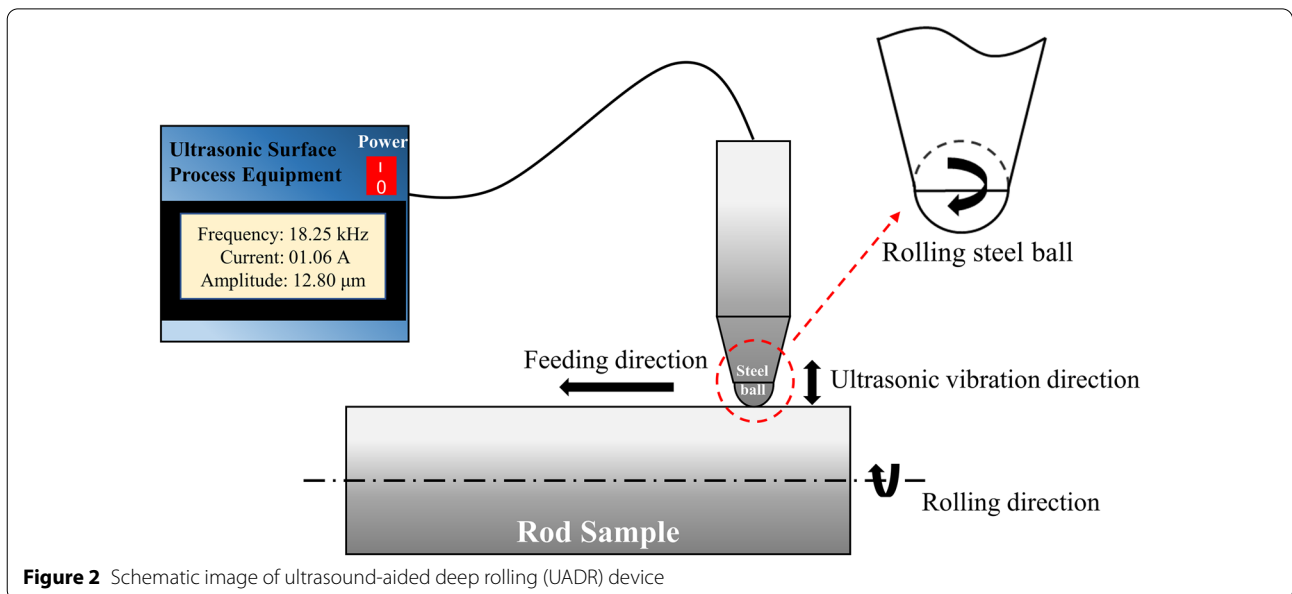


**Table 1** Chemical composition of pure Ni (N4) (mass fraction /%)

Ni+Co	C	S	P	Cu	Fe	Si	Mn	Zn
≥ 99.9	0.009	< 0.001	0.009	0.008	0.018	0.031	0.023	< 0.001



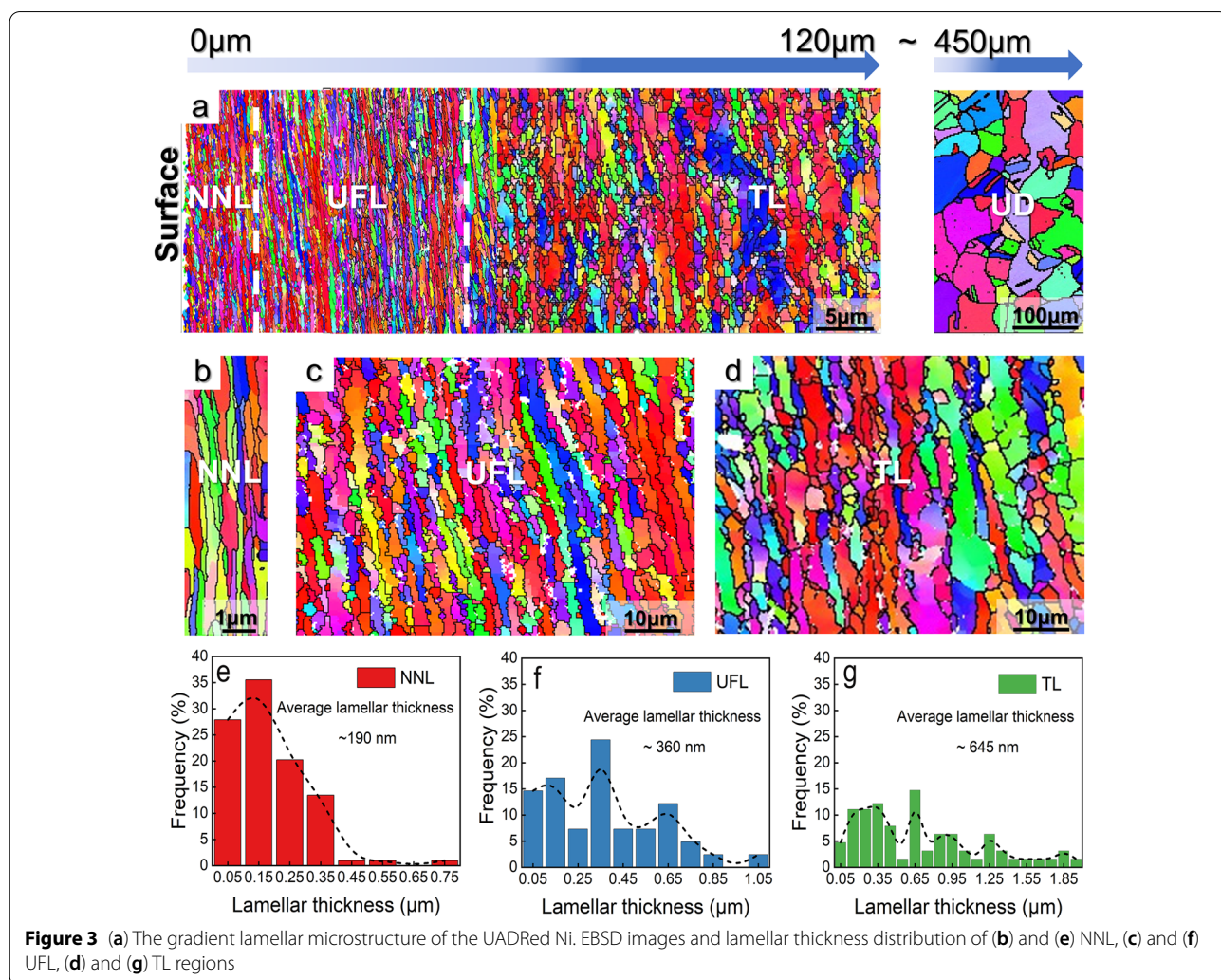
### 2.3 Microstructural Characterization

After being polished, cross-sectional microstructure of the UADRed pure Ni rod (Figure 3(a)) was analyzed by EBSD technique at 20 kV acceleration voltage with a working distance of 18 mm. The SEM imaging of the samples was conducted using the Zeiss Crossbeam 340 FIB/SEM System at the voltage of 6 kV. Before in-situ compression tests, details of microstructure along the depth can be observed through EBSD images as shown in Figures 3(b)–(d). In addition, the TEM sheets were prepared from each compressed micropillar in the SEM/FIB chamber. After thinning process, the TEM sheet with the thickness around 100 nm was processed and characterized by the FEI Talos 200X TEM system with the accelerate voltage of 200 kV.

### 2.4 In-situ Compression Tests

In-situ uniaxial micro-compression tests were performed in a Carl Zeiss CossBeam340 SEM using a

Brukers-Hysitron PI88 PicoIndenter under displacement control. The cylinder indenter was equipped with a 5 μm diameter diamond flat-punch indenter, which was much larger than the 2 μm micropillars in this work to subtract the effect of indenter on deformation behavior. Micropillars were prepared by focused ion beam (FIB) technique at 30 kV with a final finishing current of 0.1 nA or 0.05 nA from each representative region of the UADRed Ni sample. The height-to-diameter aspect ratio of micropillars was kept at 2–2.3 to avoid buckling during compression. Diameters of micropillars were the average values of top and bottom diameters measured from the SEM images, in favor of alleviating the effect of approximately 3° taper of micropillars. Micropillars were compressed at a constant strain rate of 10<sup>-3</sup> s<sup>-1</sup> to roughly 25% strain, followed by a 1 s holding before unloading. In order to ensure the reliability and repeatability of the tests, in-situ micro-compression tests were repeated 5 times for each region. The most representative curves of 5 times tests



for each region were chosen to discuss the deformation behavior in the following chapters. The force and displacement data of compression test was acquired by a piezoelectric actuator in the capacitive transducer. SEM probe monitors the compression behavior of micropillars and automatically generates real-time videos at any time.

As mentioned above, considering the existence of a slight taper, the micropillar diameters was acquired by averaging the diameters of top and bottom of micropillars to calculate the engineering stress. Moreover, in order to avoid the impact of indenter and basement below the micropillar on elastic deformation data and acquire a relatively accurate measurement of strain, the equation of a cylindrical punch derived by Frick et al. [28, 29] was applied to calculate displacement  $x$ ,

$$x = x_{meas} - \frac{1 - \nu_i^2}{E_i} \left( \frac{F_{meas}}{D_t} \right) - \frac{1 - \nu_b^2}{E_b} \left( \frac{F_{meas}}{D_b} \right), \quad (1)$$

where  $x_{meas}$  and  $F_{meas}$  represent the measured displacement and force, respectively.  $D_t$  and  $D_b$  are the diameters of top and bottom of micropillar, respectively.  $\nu_i$  and  $E_i$  are the Poisson's ratio and Young's modulus of diamond flat-punch taken to be 0.07 and 1220 GPa, respectively, while  $\nu_b$  and  $E_b$  represent the Poisson's ratio and Young's modulus of Ni selected as 0.31 and 207 GPa, respectively. Once the displacement was corrected, the engineering stress-strain curves were obtained, and subsequently converted to true stress-strain curves by using the homogeneous deformation model (assuming no volume change during the deformation).

For micropillars with smooth stress-strain curves, since the determination of the exact value of yield stress is difficult due to a continuous transition from elastic to elastoplastic deformation regimes of the stress-strain response, flow stress obtained by a strain offset of 1% instead of a conventional 0.2% offset stress, is designated as yield stress [30], as illustrated in Figures 4–6. For micropillars showing discontinuous flow behavior, the yield stress is identified as the stress at the first discrete displacement burst that occurred post-1% strain in each curve, and a threshold of  $\Delta\varepsilon \geq 0.002$  is used to identify the burst events [31], as exhibited in Figure 7(a). In this study, the strain hardening rate (SHR) is defined as the slope between the true stress–strain data at yielding point,  $\varepsilon_y$ , and 10% strain due to the strain bursts during the stress–strain response of the micropillars. If there is a strain burst at the nominal strain value, the peak stress in the burst is used.

### 3 Results

#### 3.1 Microstructure of the UADRed Ni Sample

The EBSD image of the UADRed Ni rod (Figure 3(a)) shows the gradient microstructure exhibiting unambiguous plastic deformation from top surface to 450  $\mu\text{m}$  along the depth. The gradient lamellar Ni can be roughly divided into four regions according to their differences in microstructurally geometrical characteristics. The depth range of the three regions in plastic deformation zone ranging from top surface to 120  $\mu\text{m}$  is respectively specified as 0–10  $\mu\text{m}$ , 10–50  $\mu\text{m}$  and 50–120  $\mu\text{m}$  from top surface. However, the UADR technique [32, 33]

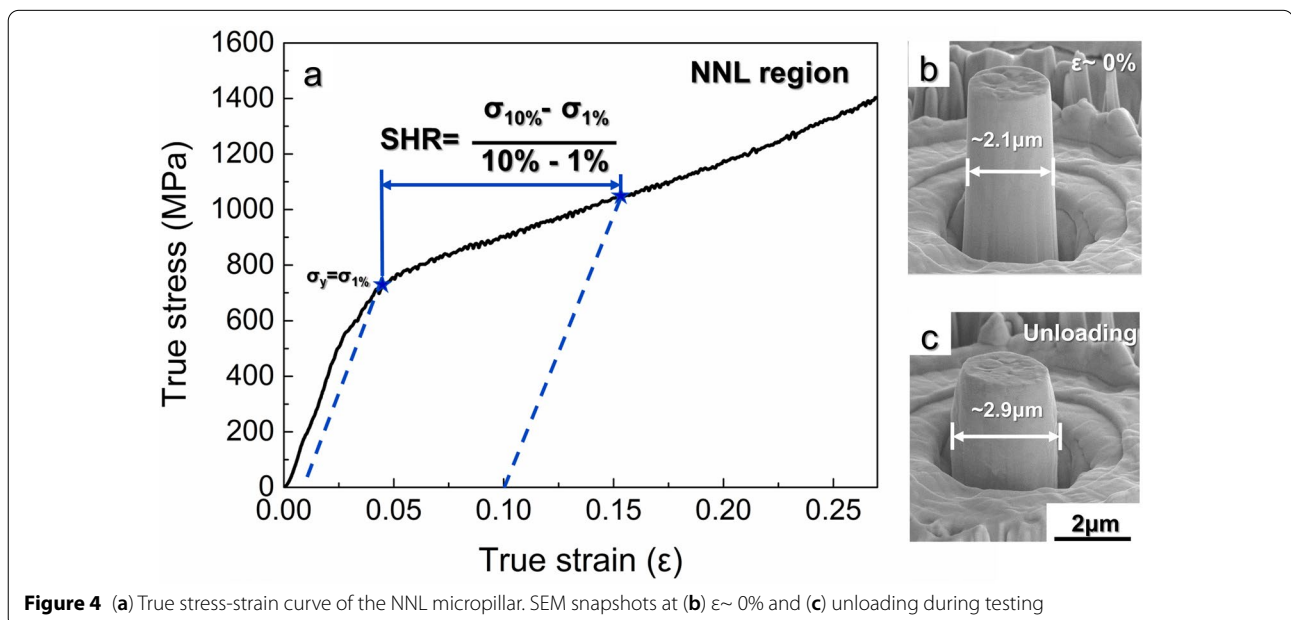


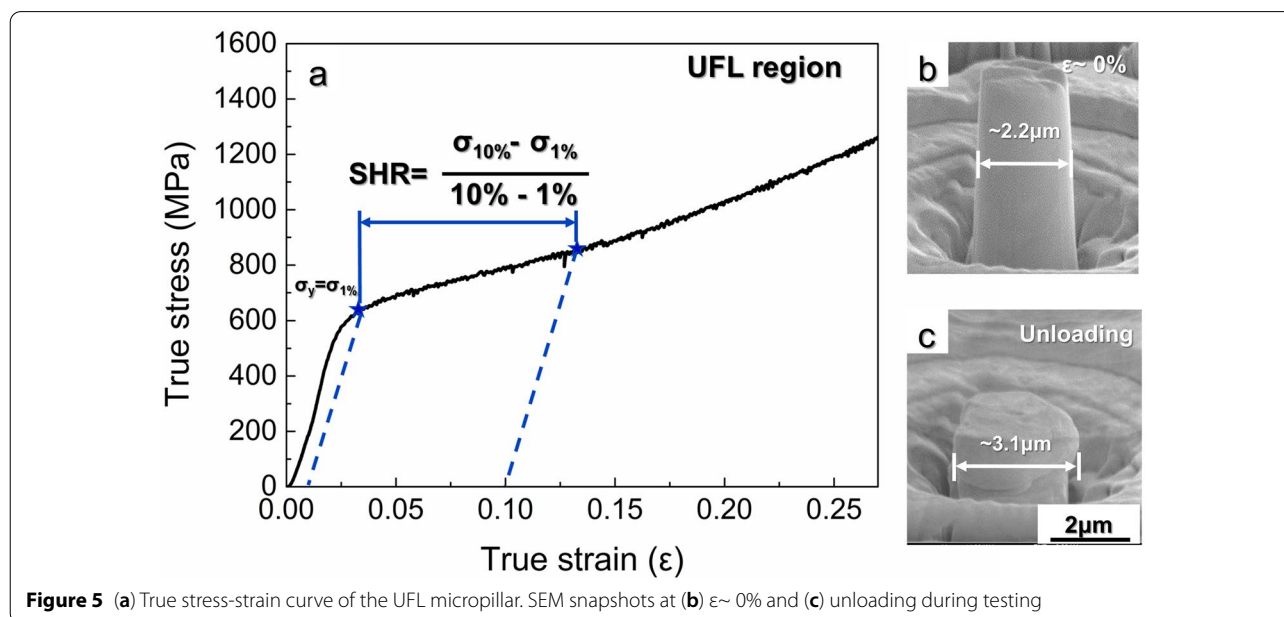
**Figure 4** (a) True stress-strain curve of the NNL micropillar. SEM snapshots at (b)  $\varepsilon \sim 0\%$  and (c) unloading during testing

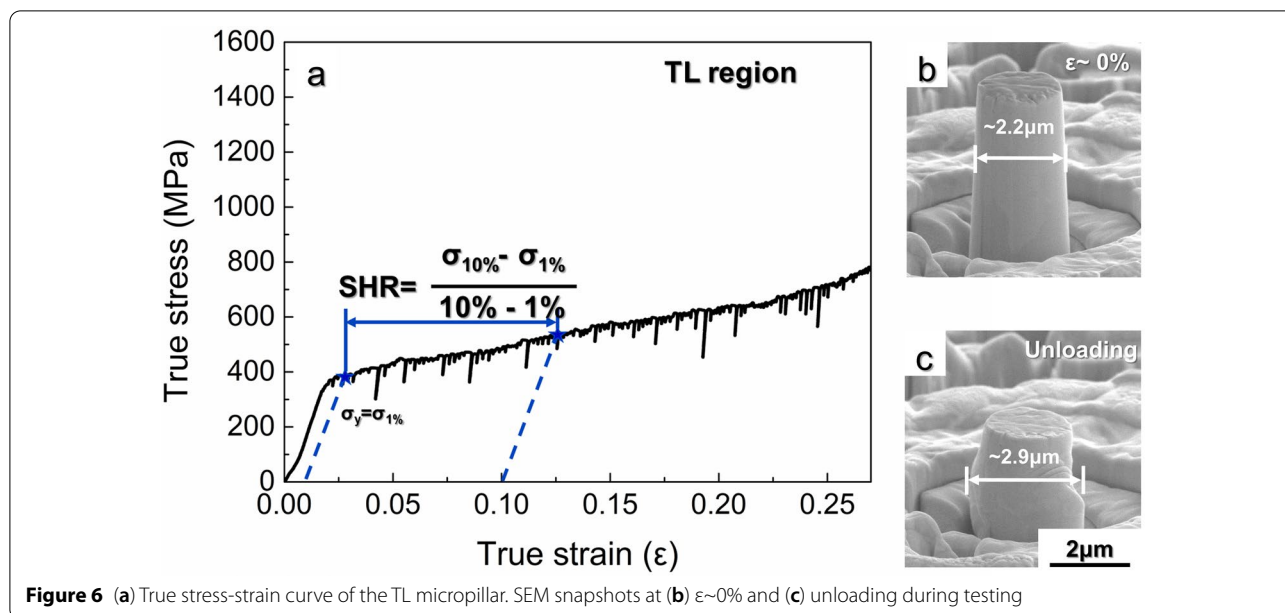
would introduce a certain extent of plastic deformation on the surface of pure Ni rod, especially the largest plastic deformation on the outermost layer, which leads that the outermost layer is difficult to be resolved under the EBSD technique [34–36]. Therefore, the microstructural details of plastic deformation regions from top surface to 6  $\mu\text{m}$  are unable to be acquired through the EBSD image shown in Figure 3(a). As shown by EBSD observation in Figure 3(b), the representative microstructural characteristic in the region ranging from 6 to 10  $\mu\text{m}$  contains near nanoscale lamellar (NNL) grains with average lamellar thickness of  $\sim 190$  nm (shown in Figure 3(e)) and hence is referred to as the NNL region. The lamellar GBs are parallel to the rolling direction. The adjacent region of 10–50  $\mu\text{m}$  from surface has severely deformed structure characterized by parallel lamellar grains named as the ultrafine lamellar (UFL) region. The elongated boundaries are also straight and flat lamellar GBs parallel to the rolling direction, which is shown in Figure 3(c). Thickness of the lamellar GBs were averagely measured as 360 nm (indicated in Figure 3(f)), and their average length is 1500  $\mu\text{m}$ . The depth range of 50–120  $\mu\text{m}$  presents sub-micron-sized grains and this range is referred to as the transition layer (TL) region, grains within TL region are elongated with an average boundary spacing of 645 nm (presented in Figure 3(g)) and length of 2  $\mu\text{m}$ . As shown in Figure 3(d), the elongated boundaries of the UFGs are inclined to the rolling direction. Finally, as shown in Figure 3(a), the average grain size of equiaxed CGs is measured about 50  $\mu\text{m}$  at the depth of 450  $\mu\text{m}$ , and region deeper than 450  $\mu\text{m}$  can be seen as the undeformed (UD) region.

### 3.2 In-situ Micropillar Compression Tests in SEM

To study different mechanical behaviors of each region, micropillars with diameter  $\sim 2$   $\mu\text{m}$  is fabricated to perform in-situ micro-compressive tests at the depth of 8  $\mu\text{m}$  (NNL), 40  $\mu\text{m}$  (UFL), 120  $\mu\text{m}$  (TL), 450  $\mu\text{m}$  (UD) from the treated surface, respectively.

From the true stress-strain curves of the NNL, UFL and TL micropillars, the NNL (Figure 4(a)) and the UFL micropillars (Figure 5(a)) were found to have a similar mechanical behavior, that is, they both deform elastically at the first stage and then get into a strain hardening stage. However, the yield stress ( $\sim 705$  MPa) and the SHR ( $\sim 2826$  MPa) of the NNL micropillar were both measured to be relatively high, while those of the UFL micropillar were measured to be 635 MPa (yield stress) and 2012 MPa (SHR), respectively. It is easy to understand that smaller lamellar grain thickness leads to higher yield stress in the NNL micropillar. Interestingly, the SHR of the NNL micropillar is still higher than the UFL micropillar, which is different from the trade-off in yield strength and the strain hardening capacity observed in other macro-scale researches [37–40]. The excellent strain hardening capacity of the NNL micropillar may result from no slip bands penetrating through micropillar surface during compression thus maintaining homogeneous plastic deformation, which could be reflected from the smooth curve (Figure 4(a)) and the post-compression SEM image (Figure 4(c)) of the NNL micropillar. Compared with the true stress-strain curve of the NNL and the UFL micropillar, the stress-strain curves of the TL micropillar (Figure 6(a)) are relatively discontinuous and apparent strain-burst appeared during compression.

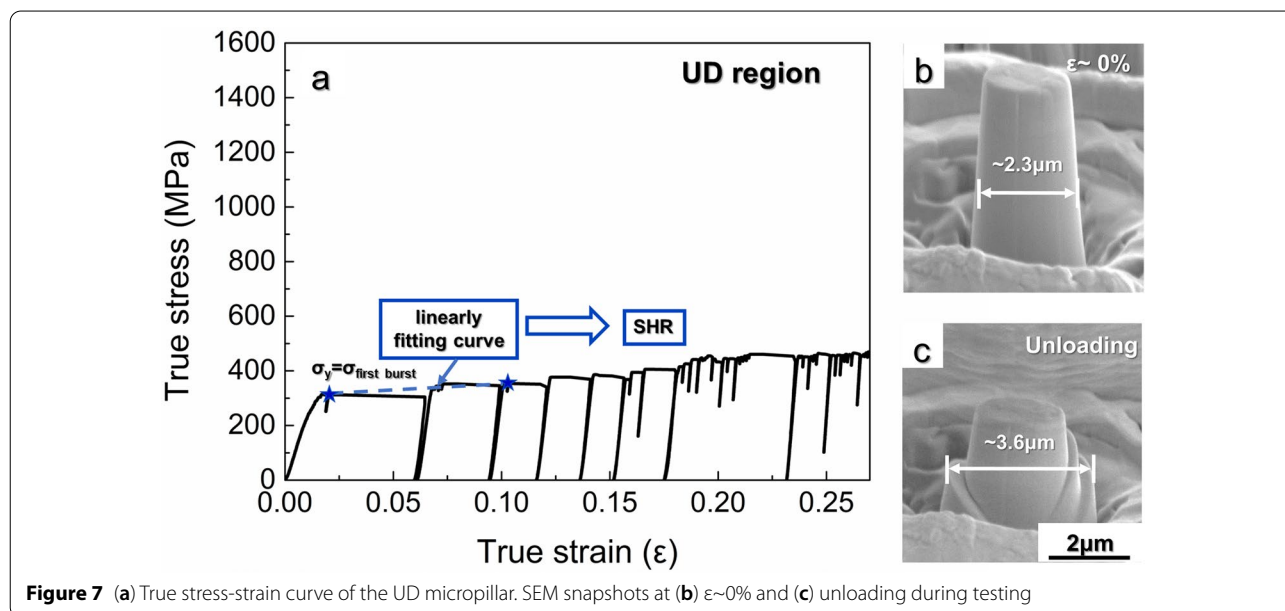




Besides, multiple slip bands were obviously observed by comparing Figure 6(b) and (c). As measured from Figure 6(a), the TL micropillar has the yield stress of 390 MPa and the SHR of 1410 MPa, both are much lower than those of the NNL and UFL micropillars.

According to the EBSD image of cross-section microstructure, the average grain size of the UD region is 50  $\mu\text{m}$ . Hence, the 2  $\mu\text{m}$  diameter micropillar fabricated from the UD region is more likely to be a single grain. The true stress-strain curve for the UD region shown in Figure 7(a) exhibits the yield strength of 310 MPa,

followed by abundant discrete ‘strain bursts’ as shown by drop in stress. Each burst is due to rapid displacement during loading [41–43], which means the flat punch tip is out of contact with the micropillar top and meanwhile stress sharply decreasing. These bursts correspond to the visible slip bands on micropillar surface shown in Figure 7(c). These slip bands existing on compressed UD micropillar are quite deep and lead to shear fracture, with length almost surround the micropillar itself. It is found that the length of slip band corresponds to the amplitude (measured as the stress increment in ascending



stage of each burst [44]) changes of strain bursts in true stress-strain curves of different micropillars. The shear fracture in compressed UD micropillar may be caused by the activation of many slip bands and then rapid penetration through the UD micropillar without the block from GBs and dislocations during compression [29, 45]. In other similar studies, the researchers have pointed out that the slip bands in the UD micropillar result from collective and avalanche-like motion of dislocations [46], which annihilate at the internal GBs or free surfaces of the micropillars [47–50]. The SHR of the UD region was measured to be 433 MPa, which was obtained by linearly fitting the peak stresses at the nominal strain values from the true stress-strain curve shown in Figure 7(a). The weak strain hardening capacity of the UD region may arise from pure slip mode without intersection of several slip systems. The phenomenon resembles deformation behavior of the CG Cu micropillar studied by Hou et al. [51], and therefore low-density defects of the CGs in the UD region are presumed to be the underlying reason for low strain hardening capacity of the micropillar in the UD region.

#### 4 Discussion

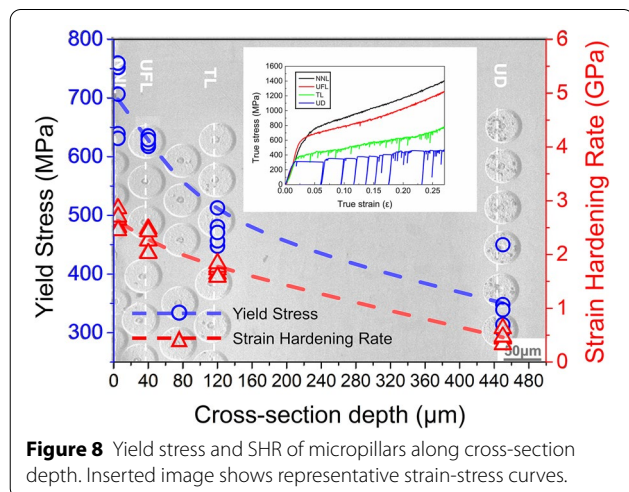
In order to compare the mechanical properties of different regions more intuitively and clearly, the yield stress and the SHR of selected five micropillars in each region are exhibited in Figure 8. Therein, the background globally exhibits the SEM image of these micropillars. Obviously, both the yield stress and the SHR monotonically increase with the decreasing depth from the treated surface. The NNL micropillar has the best combination of yield strength and strain hardening capacity. According to previous studies [52–55] on the deformation behavior of metallic materials, the deformation mode of materials

with high stacking fault energy is mainly dislocation and slip, while materials with low stacking fault energy is deformation twinning. In this work, pure Ni was employed with high stacking fault energy, and therefore micropillars in all regions deformed plastically mainly resulting from the motion of dislocation and slip rather than twins. To understand mechanisms responsible for differences in mechanical behaviors, micropillars from the four regions were respectively characterized by SEM and TEM technique. Thus, deformation mechanisms for different micropillars were analyzed from the perspective of slip and dislocation, respectively.

##### 4.1 The Effect of Slip and Lamellar GB Thickness on Strength-Plasticity

As mentioned above, the NNL micropillar consists of grains with the smallest lamellar thickness compared to other micropillars fabricated from other regions, contributing to the most GBs to block the motion of slip band. Therefore, the highest yield strength occurs in the NNL micropillar, consistent with the classical Hall-Petch effect that the strength of metallic materials increases significantly with the decrease of grain size [56, 57].

During the in-situ compression tests, the whole deformation process was recorded and the SEM images of different micropillars were exhibited in Figure 9 at specific strains ~ 0%, 10 %, 20 % and after unloading, respectively. As shown in the SEM images in Figure 9(a)–(d), the NNL micropillar exhibits a relatively homogeneous deformation from top to bottom sections of the micropillar without appearance of any shear slip band during the whole compression test. Conversely, slip system has been activated at strain ~ 20%, where some kinks emerging on the surface of the UFL micropillar are observed during compressive deformation (Figure 9(g)). Moreover, the SEM images (Figure 9(j)) of the TL micropillar show multiple slip bands parallel to each other at strain ~ 10%, which are very short and shallow. Significantly, as shown in Figure 9(n)–(p), it is found that localized shear fractures are responsible for the failure mechanism in the UD region, while the micropillars in other regions simply exhibit deformation rather than shear fracture. From the SEM images of all micropillars after compression test, it is visible that appreciable lateral bulge took place in all samples, which implies that the micropillars experienced plastic deformation during compression. However, lateral bulge in the NNL micropillar is distributed more uniformly than in the other micropillar, indicating that the plastic strain is accommodated homogeneously by the whole NNL micropillar rather than localized on one or several slip systems in other micropillars. It is speculated that many different slip systems are required to be activated in each grain aiming to coordinate with



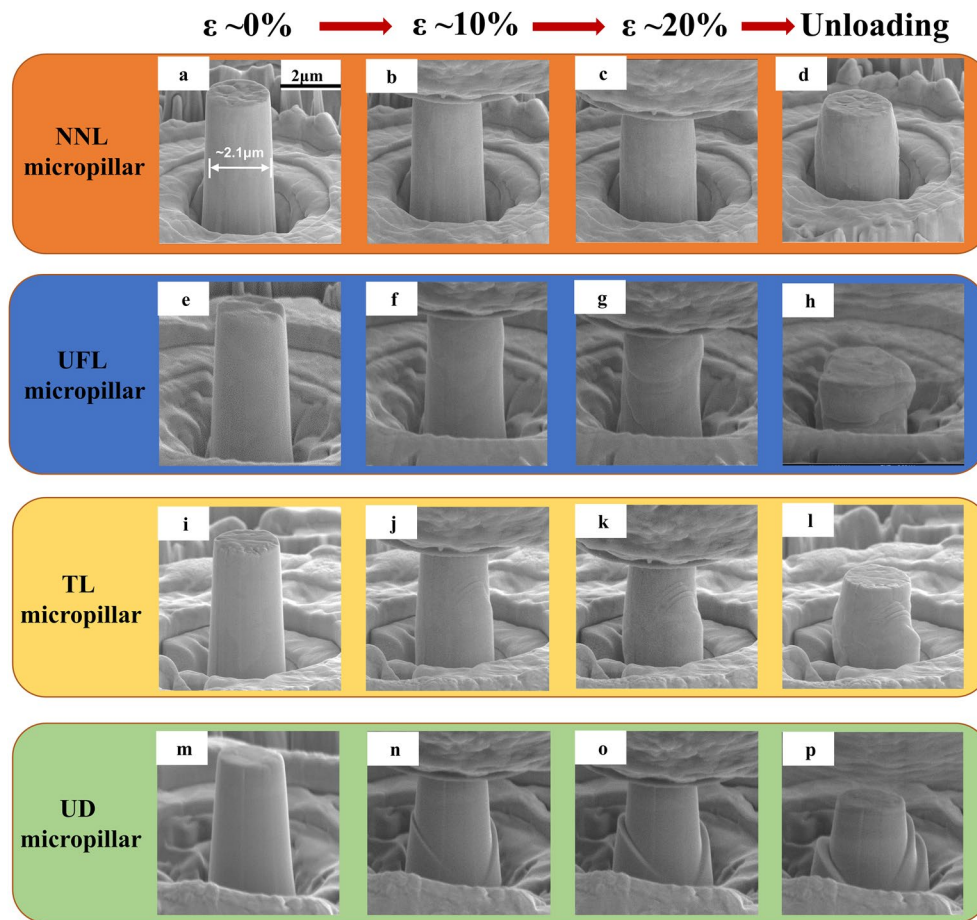


**Figure 9** SEM snapshots of the (a)–(d) NNL, (e)–(h) UFL, (i)–(l) TL and (m)–(p) UD micropillar evolution during testing

deformation of their many adjacent grains in the NNL micropillar. Consequently, the activation of many different slip systems needs extremely high applied stress, leading to the most obvious strain hardening phenomenon in the NNL micropillar. Also, these different slip bands block the slip activities from each other and distribute uniformly through the whole micropillar, resulting in no apparent strain localization to penetrate through the whole NNL micropillar or form shear fracture. Thus, the NNL micropillar exhibits not only high strength but also good plasticity compared to other micropillars.

#### 4.2 The Effect of Dislocation and Lamellar GB Orientation on Strength-plasticity

For further exploring the deformation mechanisms for micropillars in different regions, the TEM characterization was adopted to observe dislocation changes of different post-compression micropillars. Figure 10(b) and (c) shows the TEM images of post-compression NNL micropillar, where the numerous lamellar GBs and extensive dislocation could be observed clearly. Therefore, the

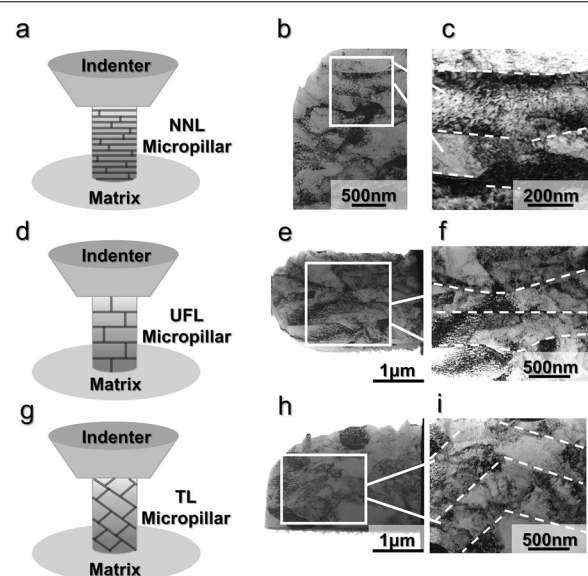


**Figure 10** Schematic images and TEM images of the (a)–(c) NNL, (d)–(f) UFL and (g)–(i) TL micropillar after testing

dislocation pile-ups in the NNL micropillar are improved due to existing lots of GBs and a great deal of dislocation interaction. Meanwhile, combined with no visible 'strain-burst' in strain-stress curves of the NNL micropillar, it is considered that no extensive dislocation annihilated on free surface of the micropillar. Additionally, the lamellar GBs are always perpendicular to the loading direction through the post-compression TEM images in the NNL micropillar. However, shear stress named critical resolved shear stress (CRSS) of a certain magnitude along the slip plane is required for the formation of slip, and the maximum resolved shear stress (MRSS) is oriented as  $45^\circ$  relative to the loading direction [48]. Therefore, the motion of many slip bands formed inside the NNL micropillar is severely blocked by perpendicular lamellar GBs, where much more stress is required to continue the generation and motion of slip bands, resulting in no visible slip band on sample surface during in-situ compression test. In summary, the  $90^\circ$  orientation with respect to the loading direction and the extensive dislocation pile-ups also contribute to the highest yield strength and the best strain hardening capacity of the NNL micropillar.

Comparing the TEM images of the UFL micropillar (Figure 10(e)) with the NNL micropillar (Figure 8(b)), it is evident that lamellar thickness is larger in the UFL micropillar with smaller yield stress. However, the lamellar GBs are still perpendicular to the loading direction. Figure 5(a)–(c) shows several slight slip bands corresponding to slight strain-burst in true stress-strain curve of the UFL micropillar, illustrating collective dislocations escaping on slip planes [58–61]. The collective escape of dislocations probably because there is no enough lamellar GBs in the UFL micropillar to block the motion of slip bands and thus several slip bands penetrate through the whole micropillar, causing the annihilation of dislocations on sample surface. Therefore, lower strain hardening capacity is obtained from the UFL micropillar compared with the NNL micropillar.

It is noted from comparing Figure 10(a), (d) and (g) that the main differences between the TL micropillar and the above two micropillars are increasing lamellar thickness, and GBs are inclined to the loading direction in the TL micropillar. As the Hall-Petch effect mentioned above, the increasing lamellar thickness leads to weak strength of the TL micropillar. However, it is worth noting that the lamellar thickness range of the TL micropillar is large, and the largest value is  $\sim 1.95 \mu\text{m}$ , which means that mainly one lamellar GB existing in the sample with diameter of  $\sim 2 \mu\text{m}$  and height of  $\sim 4 \mu\text{m}$ . Therefore, the Hall-Petch effect could not be suitable for revealing the strengthening mechanism of the TL micropillar with only one lamellar GB. In this case, the weak strength of the TL micropillar may be due to lacking GBs to block

the motion of dislocation and leading to abundant annihilation of dislocations on the sample surface. In addition, it is found that much fewer dislocations distribute in the TL micropillar compared to the NNL and the UFL micropillars, as shown in Figure 10(h). The much fewer GBs and dislocations leads to the rapid propagation of slip band in the TL micropillar, which means only one or few slip system is required to activate for maintaining plastic deformation. Thus, no interaction of many slip systems to block the further and rapid propagation of slip bands, resulting in slip bands penetrating through the whole micropillar and forming shear fracture rapidly. Moreover, the phenomenon that GBs are inclined to the loading direction indicates the lamellar GBs in the TL micropillar are affected by MRSS on  $45^\circ$  orientation. Specifically, the inclined lamellar GBs are conducive to form lots of slip bands and unable to effectively divert and prevent the propagation of slip bands in the TL micropillar, thus many slip bands propagate to the micropillar surface along the  $45^\circ$  orientation without any barrier. Consequently, abundant dislocations are annihilated on the TL micropillar surface. This is consistent with the existing abundant strain-burst observed from true strain-stress curve and visible slip bands parallel to each other on the surface of the TL micropillar. Therefore, these differences are mainly responsible for the weak strength and the poor strain hardening capacity of the TL micropillar.

## 5 Conclusions

Gradient lamellar Ni is fabricated successfully using an ultrasound-aided deep rolling technique at ambient temperature. The microstructure of gradient lamellar Ni is successively classified as the NNL, the UFL, the TL and the UD region with the increasing depth from the treated surface. In-situ micropillar compression tests are respectively performed in different regions to explore their mechanical properties. Various microstructural characterization techniques were used to thoroughly investigate their deformation mechanisms. The main conclusions can be summarized as follows.

- (1) With the decrease of lamellar GB thickness, the deformation of micropillar becomes more and more homogeneous during compression, which is reflected in the stress-strain curve, that is, the number and the amplitude of strain-burst are both decreasing.
- (2) The strength of the NNL micropillar is much larger than that of the UD micropillar because quite more lamellar GBs and initial dislocations as well as multiple slip bands block the dislocation activities in the NNL micropillar.

(3) Strain hardening capacity is related to the depth from treated surface, and smaller depth would lead to greater strain hardening capacity. This behavior may be due to multiple slip systems activated in each grain from the NNL micropillar to coordinate plastic deformation with adjacent grains while only single slip activity required in the UD micropillar leading to localized shear fracture. Meanwhile, higher strain hardening capacity is achieved when lamellar GBs are oriented at 90° rather than 45° or 0° relative to the loading direction.

#### Acknowledgements

The authors sincerely thanks to Professor Yan of East China University of Science and Technology for his critical discussion and reading during manuscript preparation.

#### Author contributions

ZMW, YFJ and XCZ conceived and designed the experiments; ZMW performed the whole experiments; ZMW and YFJ wrote the paper. All authors assisted with sampling and laboratory analyses. All authors read and approved the final manuscript.

#### Author's information

Zimeng Wang, born in 1996, is currently a PhD candidate at *Key Laboratory of Pressure Systems and Safety, Ministry of Education, School of Mechanical and Power Engineering, East China University of Science and Technology, China*.

She received her bachelor degree from *North China Electric Power University, China*, in 2017. Her research interests include material design and mechanical behavior research. Tel: +86-13851559915; E-mail: 1300993159@qq.com; Y20170068@mail.ecust.edu.cn

Yunfei Jia, born in 1986, is currently an associate professor at *Key Laboratory of Pressure Systems and Safety, Ministry of Education, School of Mechanical and Power Engineering, East China University of Science and Technology, China*. He received his PhD degree from *East China University of Science and Technology, China*, in 2014. His main research is bionic structure design and manufacture. E-mail: yfjia@ecust.edu.cn

Yong Zhang, born in 1995, is currently a PhD candidate at *Key Laboratory of Pressure Systems and Safety, Ministry of Education, School of Mechanical and Power Engineering, East China University of Science and Technology, China*. E-mail: Y20170073@mail.ecust.edu.cn

Pei Tang, born in 1997, is currently a master candidate at *Key Laboratory of Pressure Systems and Safety, Ministry of Education, School of Mechanical and Power Engineering, East China University of Science and Technology, China*. E-mail: 1284807626@qq.com

Xiancheng Zhang, born in 1979, is currently a professor at *Key Laboratory of Pressure Systems and Safety, Ministry of Education, School of Mechanical and Power Engineering, East China University of Science and Technology, China*. He received his PhD degree from *Shanghai Jiao Tong University, China*, in 2007. He focuses on research about safety theory and technology of high temperature structure. E-mail: xc Zhang@ecust.edu.cn

Shantung Tu, born in 1961, is currently a professor at *Key Laboratory of Pressure Systems and Safety, Ministry of Education, School of Mechanical and Power Engineering, East China University of Science and Technology, China*. He received his PhD degree from *Nanjing Tech University, China*, in 1988. His main research is chemical equipment safety, high temperature intensity and so on. E-mail: sttu@ecust.edu.cn

#### Funding

Supported by National Key Research and Development Program of China (Grant No. 2018YFC1902404), National Natural Science Foundation of China (Grant No. 51975211, 51725503), Innovation Program of Shanghai Municipal

Education Commission (Grant No. 2019-01-07-00-02-E00068), and 111 Project, Shanghai Rising-Star Program (Grant No. 20QA1402500)

#### Competing interests

The authors declare no competing financial interests.

Received: 19 December 2021 Revised: 11 April 2022 Accepted: 22 April 2022

Published online: 26 May 2022

#### References

- [1] J Hu, Y N Shi, X Sauvage, et al. Grain boundary stability governs hardening and softening in extremely fine nanograined metals. *Science*, 2017, 355(6331): 1292-1296.
- [2] K Lu. Making strong nanomaterials ductile with gradients. *Science*, 2014, 345(6203): 1455-1456.
- [3] K S Kumar, H Van Swyghoven, S Suresh. Mechanical behavior of nanocrystalline metals and alloys. *Acta Materialia*, 2003, 51(19): 5743-5774.
- [4] Y M Wang, E Ma. Strain hardening, strain rate sensitivity, and ductility of nanostructured metals. *Materials Science & Engineering A*, 2004, 375-377(1): 46-52.
- [5] M Yang, Y Pan, F Yuan, et al. Back stress strengthening and strain hardening in gradient structure. *Materials Research Letters*, 2016, 4(3): 145-151.
- [6] Y Wei, Y Li, L Zhu, et al. Evading the strength-ductility trade-off dilemma in steel through gradient hierarchical nanotwins. *Nature Communications*, 2014, 5(4): 3580.
- [7] H W Zhang, X Huang, N Hansen. Evolution of microstructural parameters and flow stresses toward limits in nickel deformed to ultra-high strains. *Acta Materialia*, 2008, 56(19): 5451-5465.
- [8] X Wu, P Jiang, L Chen, et al. Extraordinary strain hardening by gradient structure. *Proceedings of the National Academy of Sciences of the United States of America*, 2014, 111(20): 7197.
- [9] X L Ma, C X Huang, W Z Xu, et al. Strain hardening and ductility in a coarse-grain/nanostructure laminate material. *Scripta Materialia*, 2015, 103: 57-60.
- [10] E Ma, T Zhu. Towards strength-ductility synergy through the design of heterogeneous nanostructures in metals. *Materials Today*, 2017, 20(6): 323-331.
- [11] X Wu, Y Zhu. Heterogeneous materials: a new class of materials with unprecedented mechanical properties. *Materials Research Letters*, 2017, 5(8): 527-532.
- [12] X Wu, M Yang, F Yuan, et al. Heterogeneous lamella structure unites ultrafine-grain strength with coarse-grain ductility. *Proceedings of the National Academy of Sciences*, 2015, 112(47): 14501-14505.
- [13] M Song, C Sun, J Jang, et al. Microstructure refinement and strengthening mechanisms of a 12Cr ODS steel processed by equal channel angular extrusion. *Journal of Alloys and Compounds*, 2013, 577: 247-256.
- [14] X C Liu, H W Zhang, K Lu. Formation of nano-laminated structure in nickel by means of surface mechanical grinding treatment. *Acta Materialia*, 2015, 96: 24-36.
- [15] A T Bozdana, N N Z Gindy. Comparative experimental study on effects of conventional and ultrasonic deep cold rolling processes on Ti-6Al-4V. *Materials Science and Technology*, 2008, 24(11): 1378-1384.
- [16] Y L Zhu, K Wang, L Li, et al. Evaluation of an ultrasound-aided deep rolling process for anti-fatigue applications. *Journal of Materials Engineering and Performance*, 2009, 18(8): 1036-1040.
- [17] X J Cao, Y S Pyoun, R Murakami. Fatigue properties of a S45C steel subjected to ultrasonic nanocrystal surface modification. *Applied Surface Science*, 2010, 256(21): 6297-6303.
- [18] M Koyama, Z Zhang, M M Wang, et al. Bone-like crack resistance in hierarchical metastable nanolaminate steels. *Science*, 2017, 355(6329): 1-3.
- [19] X Bian, F Yuan, Y Zhu, et al. Gradient structure produces superior dynamic shear properties. *Materials Research Letters*, 2017, 5(7): 501-507.
- [20] S V Konovikhin, D Y Kovalev, A E Sytschev, et al. Formation of nanolaminate structures in the Ti-Si-C system: A crystallochemical study. *International Journal of Self-Propagating High-Temperature Synthesis*, 2014, 23(4): 217-221.

- [21] Y Zhao, T Topping, J F Bingert, et al. High tensile ductility and strength in bulk nanostructured nickel. *Advanced Materials*, 2008, 20(16): 3028–3033.
- [22] B Q Han, J Y Huang, Y T Zhu, et al. Strain rate dependence of properties of cryomilled bimodal 5083 Al alloys. *Acta Materialia*, 2006, 54(11): 3015–3024.
- [23] C Sawangrat, S Kato, D Orlov, et al. Harmonic-structured copper: performance and proof of fabrication concept based on severe plastic deformation of powders. *Journal of Materials Science*, 2014, 49(19): 6579–6585.
- [24] S K Vajpai, M Ota, T Watanabe, et al. The development of high performance Ti-6Al-4V Alloy via a unique microstructural design with bimodal grain size distribution. *Metallurgical and Materials Transactions A*, 2015, 46(2): 903–914.
- [25] L Li, Y Zhu, G Lue. Influence of ultrasonic deep rolling on reducing surface roughness and healing surface scar of TC4 Titanium Alloy. *Rare Metal Materials and Engineering*, 2009, 38(2): 339–342.
- [26] G D Shao, H W Li, M Zhan. A review on ultrasonic-assisted forming: Mechanism, model, and process. *Chinese Journal of Mechanical Engineering*, 2021, 34: 99.
- [27] S Guo, W Du, Q H Jiang, et al. Surface integrity of ultrasonically-assisted milled Ti6Al4V Alloy manufactured by selective laser melting. *Chinese Journal of Mechanical Engineering*, 2021, 34: 67.
- [28] C P Frick, B G Clark, S Orso, et al. Size effect on strength and strain hardening of small-scale [111] nickel compression pillars. *Materials Science and Engineering: A*, 2008, 489(1–2): 319–329.
- [29] J Ding, Q Li, J Li, et al. Mechanical behavior of structurally gradient nickel alloy. *Acta Materialia*, 2018, 149: 57–67.
- [30] J A Lee, M Y Seok, Y K Zhao, et al. Statistical analysis of the size- and rate-dependence of yield and plastic flow in nanocrystalline copper pillars. *Acta Materialia*, 2017, 127: 332–340.
- [31] Y H Hu, Q Guo, L Zhao, et al. Correlating micro-pillar compression behavior with bulk mechanical properties: Nanolaminated graphene-Al composite as a case study. *Scripta Materialia*, 2018, 146: 236–240.
- [32] A Tolga Bozdana, N N Z Gindy, H Li. Deep cold rolling with ultrasonic vibrations—a new mechanical surface enhancement technique. *International Journal of Machine Tools and Manufacture*, 2005, 45(6): 713–718.
- [33] M Yasuoka, P Wang, K Zhang, et al. Improvement of the fatigue strength of SUS304 austenite stainless steel using ultrasonic nanocrystal surface modification. *Surface and Coatings Technology*, 2013, 218: 93–98.
- [34] Y M Huang, C X Pan. Micro-stress-strain analysis in materials based upon EBSD technique: a review. *Journal of Chinese Electron Microscopy Society*, 2010, 29(1): 1–11.
- [35] A J Wilkinson, D J Dingley. Quantitative deformation studies using electron back scatter patterns. *Acta Metallurgica et Materialia*, 1991, 39(12): 3047–3055.
- [36] M Kamaya. Measurement of local plastic strain distribution of stainless steel by electron backscatter diffraction. *Materials Characterization*, 2009, 60(2): 125–132.
- [37] C A Schuh, T G Nieh, T Yamasaki. Hall–Petch breakdown manifested in abrasive wear resistance of nanocrystalline nickel. *Scripta Materialia*, 2002, 46(10): 735–740.
- [38] W Pachla, M Kulczyk, M Sus-Ryszkowska, et al. Nanocrystalline titanium produced by hydrostatic extrusion. *Journal of Materials Processing Technology*, 2008, 205(1): 173–182.
- [39] C C Koch. Optimization of strength and ductility in nanocrystalline and ultrafine grained metals. *Scripta Materialia*, 2003, 49(7): 657–662.
- [40] C A Schuh, T G Nieh, H Iwasaki. The effect of solid solution W additions on the mechanical properties of nanocrystalline Ni. *Acta Materialia*, 2003, 51(2): 431–443.
- [41] E M Grieveson, D E J Armstrong, S Xu, et al. Compression of self-ion implanted iron micropillars. *Journal of Nuclear Materials*, 2012, 430(1–3): 119–124.
- [42] P Wang, F Liu, Y Cui, et al. Interpreting strain burst in micropillar compression through instability of loading system. *International Journal of Plasticity*, 2018, 107: 150–163.
- [43] Q Jiao, J Cheng, G D Sim, et al. Micro-mechanical investigation of the thermo-mechanical properties of micro-architected tungsten coatings. *Journal of the Mechanics and Physics of Solids*, 2021, 150: 104326.
- [44] M Zaiser, J Schwerdtfeger, A S Schneider, et al. Strain bursts in plastically deforming molybdenum micro- and nanopillars. *Philosophical Magazine*, 2008, 88(30–32): 3861–3874.
- [45] Y Zhao, J Zhang, Y Wang, et al. The metastable constituent effects on size-dependent deformation behavior of nanolaminated micropillars: Cu/FeCoCrNi vs Cu/CuZr. *Journal of Materials Science & Technology*, 2021, 68: 16–29.
- [46] F F Csikor, C Motz, D Weygand, et al. Dislocation Avalanches, Strain Bursts, and the Problem of Plastic Forming at the Micrometer Scale. *Science*, 2007, 318(5848): 251–254.
- [47] A Kunz, S Pathak, J R Greer. Size effects in Al nanopillars: Single crystalline vs. bicrystalline. *Acta Materialia*, 2011, 59(11): 4416–4424.
- [48] S Feng, Q Guo, Z Li, et al. Strengthening and toughening mechanisms in graphene-Al nanolaminated composite micro-pillars. *Acta Materialia*, 2017, 125: 98–108.
- [49] Y N Cui, Z L Liu, Z J Wang, et al. Mechanical annealing under low-amplitude cyclic loading in micropillars. *Journal of the Mechanics and Physics of Solids*, 2016, 89: 1–15.
- [50] H Guo, X Zhang, F Shang, et al. A modified single-arm source model for the size-dependent strain-hardening behavior of metallic micropillars. *International Journal of Mechanical Sciences*, 2017, 133: 438–448.
- [51] X D Hou, S Krauss, B Merle. Additional grain boundary strengthening in length-scale architected copper with ultrafine and coarse domains. *Scripta Materialia*, 2019, 165: 55–59.
- [52] R Pippin, S Scherriau, A Taylor, et al. Saturation of fragmentation during severe plastic deformation. *Annual Review of Materials Research*, 2010, 40(1): 319–343.
- [53] T G Langdon. Twenty-five years of ultrafine-grained materials: Achieving exceptional properties through grain refinement. *Acta Materialia*, 2013, 61(19): 7035–7059.
- [54] G Mohanty, J Wehrs, B L Boyce, et al. Room temperature stress relaxation in nanocrystalline Ni measured by micropillar compression and miniature tension. *Journal of Materials Research*, 2016, 31(8): 1085–1095.
- [55] R Maass, M D Uchic. In-situ characterization of the dislocation-structure evolution in Ni micro-pillars. *Acta Materialia*, 2012, 60(3): 1027–1037.
- [56] E O Hall. The deformation and ageing of mild steel: III discussion of results. *Proceedings of the Physical Society. Section B*, 1951, 64(9): 747.
- [57] N J Petch. The cleavage strength of polycrystals. *Journal of the Iron and Steel Institute*, 1953, 174(12): 25–28.
- [58] X X Zhao, J Wu, Y L Chiu, et al. Critical dimension for the dislocation structure in deformed copper micropillars. *Scripta Materialia*, 2019, 163: 137–141.
- [59] D Kiener, A M Minor. Source truncation and exhaustion: insights from quantitative in situ TEM tensile testing. *Nano Letters*, 2011, 11(9): 3816–3820.
- [60] G Dehm, B N Jaya, R Raghavan, et al. Overview on micro- and nanomechanical testing: New insights in interface plasticity and fracture at small length scales. *Acta Materialia*, 2018, 142: 248–282.
- [61] J D Gravell, S Lee, S Ryu, et al. Effect of size and orientation on stability of dislocation networks upon torsion loading and unloading in FCC metallic micropillars. *Acta Materialia*, 2021, 214: 117010.

Submit your manuscript to a SpringerOpen<sup>®</sup> journal and benefit from:

- Convenient online submission
- Rigorous peer review
- Open access: articles freely available online
- High visibility within the field
- Retaining the copyright to your article

Submit your next manuscript at ► [springeropen.com](https://www.springeropen.com)